Dynamical properties and secondary decay effects of projectile fragmentations in ^{124}Sn,^{107}Sn + ^{120}Sn collisions at 600 MeV/nucleon

Jun Su,[1,*] W. Trautmann,[2] Long Zhu,[1] Wen-Jie Xie,[3,4] and Feng-Shou Zhang[5,6,7]

[1]*Sino-French Institute of Nuclear Engineering and Technology, Sun Yat-sen University, Zhuhai 519082, China*

[2]*GSI Helmholtzzentrum für Schwerionenforschung GmbH, D-64291 Darmstadt, Germany*

[3]*Department of Physics, Yuncheng University, Yuncheng 044000, China*

[4]*Institute of Modern Physics, Chinese Academy of Sciences, Lanzhou 730000, China*

[5]*The Key Laboratory of Beam Technology and Material Modification of Ministry of Education, College of Nuclear Science and Technology, Beijing Normal University, Beijing 100875, China*

[6]*Beijing Radiation Center, Beijing 100875, China*

[7]*Center of Theoretical Nuclear Physics, National Laboratory of Heavy Ion Accelerator of Lanzhou, Lanzhou 730000, China*

(Received 14 November 2017; revised manuscript received 7 March 2018; published 18 July 2018)

Background: Projectile fragmentation is a well-established technique to produce rare isotope beams, but its underlying physical processes are not fully known.

Purpose: We devote ourselves to studying the dynamical properties and secondary decay effects of projectile fragmentations in ^{124}Sn, ^{107}Sn + ^{120}Sn collisions at 600 MeV/nucleon.

Method: The formation of the projectile spectator and the fragmentation process are studied with the isospin-dependent quantum molecular dynamics (IQMD) model. The minimum spanning tree algorithm and the ratio of parallel to transverse quantities are applied to distinguish the equilibrated projectile spectator during the dynamics evolution. The influence of secondary decay on fragmentation observables is investigated by comparing the calculations with and without the statistical code GEMINI. The validity of the theoretical approach is tested by comparing the calculated product yields with the experimental results of the ALADIN Collaboration for the studied reactions.

Results: The general correlation of an increasing excitation energy with a decreasing mass of the spectator system is found for collisions with impact parameter of $b = 5$–10 fm. The nucleon evaporation of the prefragments reduces the multiplicity of intermediate-mass fragments, but does not change their dependence on the isospin of the projectile. The sequential decay also leads to narrower isotope distributions. Switching to GEMINI at a higher excitation energy results in slightly narrower isotope distributions. With the GEMINI code, in which the nuclear masses with shell and pairing corrections are adopted, the calculations can rather generally reproduce the data of the isotope distributions and mean neutron-to-proton ratios of the light fragments.

Conclusion: By permitting only evaporation in GEMINI, the IQMD+GEMINI model is able to reproduce the main features of projectile fragmentation in the studied Sn+Sn reactions.

DOI: 10.1103/PhysRevC.98.014610

I. INTRODUCTION

Nuclear fragmentation, in which several intermediate-mass fragments (IMFs) are produced, has been the subject of many experimental and theoretical works [1–3]. It was observed in nearly all types of high-energy nuclear reactions induced by hadrons, photons, and heavy ions [4,5]. According to the participant-spectator model [6], the overlapping region between the projectile and target in heavy-ion collisions (HICs) is called the participant, while the remaining parts are called the spectators. The projectile spectator, to which a fraction of the available energy is transferred, may decay by nuclear fragmentation. This process is called projectile fragmentation. The projectile fragmentation leads to the emission of fragments with a broad mass region from nucleons to fragments as heavy as the initial projectile, and a broad isospin region from neutron-deficient to neutron-rich isotopes [7,8]. In addition, the fragments from the projectile fragmentation have a momentum per nucleon almost equal to that of the projectile and are emitted into a narrow cone around the beam direction. Thus, the projectile fragmentation is a well-established technique to produce rare isotope beams in many of the present and next-generation radioactive beam facilities [9,10].

From the point of view of basic science, understanding projectile fragmentation is important not only to study the reaction mechanism of nuclear collisions [11,12], but also to extract the nuclear equation of state [13]. Since the pioneering work at Berkeley in the 1970s [14,15], the reaction mechanism of projectile fragmentation has been studied extensively. Some observables, such as production cross sections [16], momentum distributions [17,18], and angular momenta [19,20] of the produced fragments, have been measured to probe the underlying reaction mechanisms. It has been found

*sujun3@mail.sysu.edu.cn

that several common characteristics are displayed in the projectile fragmentation at high incident energies. For example, many experimental observables in peripheral collisions at high energies (>200 MeV/nucleon), such as mass, charge, and multiplicity distributions, vary little with energy and target material [3]. Some other quantities, such as excitation energy, mass, and angular momenta of the projectile spectator, are necessary to form a complete picture of the process [21]. However, the determination of these characteristics cannot be straightforward from the experimental data.

Several models have been developed to describe the underlying physical processes in HICs at intermediate energies. Phenomenological models, such as EPAX [16,22], COFRA [23,24], and FRACS [25], are developed relying on existing data and hence can predict reasonably accurate cross sections for productions. Statistical models are developed by subdividing the HICs into a dynamical stage leading to the formation of an equilibrated nuclear system and a statistical stage emitting the fragments. Examples of the statistical models are the statistical abrasion ablation model [26], the statistical multifragmentation model (SMM) [27], the canonical thermodynamic model [28,29], and the GEMINI code [30]. In order to start the statistical models, it is necessary to know the charge, mass, excitation energy, and cross section of the excited projectile system. These quantities can be calculated using straight line trajectories for the projectile and the target, or obtained with the intranuclear cascade approach. Alternatively, transport models, such as Boltzmann-Uehling-Uhlenbeck (BUU) models [31] and the isospin-dependent quantum molecular dynamics (IQMD) model [32], are applied to calculate the properties and fragmentation of the abraded system [33–35]. Recently, powerful and elaborate calculations for the projectile fragmentation were also made by transport models like the heavy-ion phase-space exploration model [36] and the antisymmetrized molecular dynamics model [37,38].

In this work, the projectile fragmentation in Sn + Sn collisions at 600 MeV/nucleon is investigated within the framework of the IQMD model [32,39] plus GEMINI code [30]. The version of the IQMD code used in this paper is IQMD-BNU (Beijing Normal University), which has been introduced and compared to other versions within the transport-code-comparison project [40,41]. Not only the properties of the projectile spectator but also the fragmentation processes are studied with the IQMD model. The GEMINI model is applied to simulate the decays of the prefragments. The paper is organized as follows. In Sec. II, we briefly describe the method. In Sec. III, we present both the results and discussions. Finally, a summary is given in Sec. IV.

II. THEORETICAL FRAMEWORK

A. Isospin-dependent quantum molecular dynamics model

The wave function for each nucleon in the IQMD model is represented by a Gaussian wave packet

$$\phi_i(\mathbf{r},t) = \frac{1}{(2\pi L)^{3/4}} e^{-\frac{[\mathbf{r}-\mathbf{r}_i(t)]^2}{4L}} e^{\frac{i\mathbf{r}\cdot\mathbf{p}_i(t)}{\hbar}}, \tag{1}$$

where $\mathbf{r}_i$ and $\mathbf{p}_i$ are the average values of the positions and momenta of the ith nucleon, and L is related to the extension of the wave packet. Note that the definition of L differs by a factor of 4 from that used in Eq. (7) of Ref. [32]. For the actual calculations, $L = 1.0$ fm^2 has been chosen. The total N-body wave function is assumed to be the direct product of these coherent states. Through a Wigner transformation of the wave function, the N-body phase-space density is given by

$$f(\mathbf{r},\mathbf{p},t) = \sum_{i=1}^{N} \frac{1}{(\pi\hbar)^3} e^{-\frac{[\mathbf{r}-\mathbf{r}_i(t)]^2}{2L}} e^{-\frac{[\mathbf{p}-\mathbf{p}_i(t)]^2\cdot 2L}{\hbar^2}}. \tag{2}$$

The time evolution of the nucleons in the system under the self-consistently generated mean field are governed by Hamiltonian equations of motion,

$$\dot{\mathbf{r}}_i = \nabla_{\mathbf{p}_i} H, \quad \dot{\mathbf{p}}_i = -\nabla_{\mathbf{r}_i} H. \tag{3}$$

The Hamiltonian of baryons in this work consists of the kinetic energy, the Coulomb interaction, and the nuclear interaction. The nuclear potential energy density of the asymmetric nuclear matter with density ρ and asymmetry δ is given by

$$V(\rho,\delta) = \frac{\alpha}{2}\frac{\rho^2}{\rho_0} + \frac{\beta}{\gamma+1}\frac{\rho^{\gamma+1}}{\rho_0^{\gamma}} + \frac{C_{sp}}{2}\left(\frac{\rho}{\rho_0}\right)^{\gamma_i}\rho\delta^2, \tag{4}$$

where ρ_0 is the normal density. The parameters α, β, γ, C_{sp}, and γ_i are temperature independent. In Eq. (4), the first and second terms refer to the local two-body and three-body interactions, which are widely used in transport models [39]. The form of the symmetry potential, shown as the third term in Eq. (4), was proposed by Tsang *et al.* [42].

The parameters used in the following work are $\alpha = 356.00$ MeV, $\beta = 303.00$ MeV, and $\gamma = 7/6$. They provide a compressibility of 200 MeV at saturation density (without momentum-dependent interactions [32]) for isospin-symmetric nuclear matter. There are several options of C_{sp} and γ_i in the IQMD code to provide different density dependencies of the symmetry energy. In this work, $C_{sp} = 38.06$ MeV and $\gamma_i = 0.75$ are used. Work is in progress to study possible consequences of varying C_{sp} and γ_i.

Binary nucleon-nucleon (NN) collisions are included in the IQMD model. The NN collisions simulate the effect of the short-range repulsive residual interaction together with the stochastic change of the phase-space distribution. The differential cross sections of NN collisions can be written as

$$\left(\frac{d\sigma}{d\Omega}\right)_i = \sigma_i^{\text{free}} f_i^{\text{angl}} f_i^{\text{med}}, \tag{5}$$

where σ^{free} is the cross section of NN collisions in free space, f^{angl} gives the angular distribution, and f^{med} gives the in-medium corrections. The subscript i is used to distinguish the channels of the NN collisions, i.e., elastic proton-proton (pp) scatterings, elastic neutron-neutron (nn) scatterings, elastic neutron-proton (np) scatterings, and inelastic NN collisions. The isospin-dependent parametrization of σ^{free} and f^{angl} adopted in this work is taken from Ref. [43]. The in-medium factor for elastic scatterings is written as [44]

$$f_{el}^{\text{med}} = \sigma_0/\sigma^{\text{free}} \tanh(\sigma^{\text{free}}/\sigma_0),$$
$$\sigma_0 = 0.85\rho^{-2/3}. \tag{6}$$

The density dependence can be seen in Eq. (6). Since the cross section in free space σ^{free} depends on the energy and

isospin, the in-medium factor is also energy dependent and isospin dependent. The authors of Ref. [44] declared that the in-medium factor does fine when checked against stopping data with the pBUU [45]. The effect of using in-medium modified cross sections is very small for the fragment observables considered here. The calculated fragment multiplicities are slightly reduced by about 9%. We do not consider the in-medium correction of inelastic *NN* collisions.

To compensate for the fermionic feature, the method of the phase-space density constraint (PSDC) in the constrained molecular dynamics (CoMD) model [46] is applied. The phase-space occupation probability $\overline{f}_i$ is calculated by performing the integration on a hypercube of volume h^3 in the phase space centered around the ith nucleon at each time step. At each time step and for each nucleon, the phase-space occupation $\overline{f}_i$ is checked. If phase-space occupation $\overline{f}_i$ has a value greater than 1, the momentum of the ith nucleon is changed randomly by many-body elastic scattering.

In the case of collisions, the Pauli blocking of the final states is taken into account. Note that in Ref. [32] collisions are allowed with the probability $(1 - f_i')(1 - f_j')$, in which f_i' and f_j' are the phase-space densities at the final states before the scattered particle is placed there. The Pauli blocking method related to the PSDC is used in the present work. These two Pauli blocking methods have been compared in our previous work [47]. The Pauli blocking method related to the PSDC is necessary after we use the PSDC method to compensate for the fermionic feature. It is required that no state with $\overline{f}_i > 1$ is created in a binary *NN* collision; otherwise it will be changed by the PSDC method. Thus, the phase-space occupation probabilities $\overline{f}_i$ and $\overline{f}_j$ at the final states are measured for each binary *NN* collision. Only if $\overline{f}_i$ and $\overline{f}_j$ at the final states are both less than 1, the scattering is accepted.

B. GEMINI

After the evolution by the IQMD code, the prefragments are formed, and the GEMINI code is switched on. The simulations of the IQMD code will be stopped when the excitation energies of the two heaviest prefragments are less than a specified value $E_{\rm stop}$. The charge number, mass number, and excitation energy of each prefragment are outputted by the IQMD code. If the excitation energy is greater than zero, the sequential decays of the prefragment will be performed by the statistical code GEMINI. It allows not only light-particle evaporation and symmetric fission, but all possible binary-decay modes. A Monte Carlo technique is employed to follow all decay chains until the resulting products are unable to undergo further decays. The partial decay widths are taken from the Hauser-Feshbach formalism for light-particle evaporation. For the emission of a light particle (Z_1, A_1) of spin J_1 from a system (Z_0, A_0) of excitation energy E^* and spin J_0, leaving the residual system (Z_2, A_2) with spin J_2, the decay width is given by

$$\Gamma_{J_2}(Z_1,A_1,Z_2,A_2) = \frac{2J_1+1}{2\pi\rho_0}\sum_{l=|J_0-J_2|}^{J_0+J_2}\int_0^{E^*-B-E_{\rm rot}} \times T_l(\varepsilon)\rho_2(E^*-B-E_{\rm rot}-\varepsilon,J_2)d\varepsilon, \quad (7)$$

where l and ε are the orbital angular momentum and kinetic energy of the emitted particle, $E_{\rm rot}$ is the rotation plus deformation energy of the residual system, ρ_0 and ρ_2 are the level densities of the initial and residual systems, respectively, and T_l is the transmission coefficient. The separation energy B is calculated from the nuclear masses. The tabulated masses are applied. The details of GEMINI are given in Ref. [30].

III. RESULTS AND DISCUSSION

A. Properties of projectile spectator

It is assumed that the multifragmentation process is subdivided into three stages. After the projectile has touched the target, a dynamical and nonequilibrium stage leads to the formation of an equilibrated projectile spectator. The excited projectile spectator disassembles into individual, possibly excited, primary fragments, and the final fragments are produced after the subsequent deexcitation of the hot primary fragments.

In the IQMD model, the positions and momenta of the nucleons as a function of time can be obtained. At any time during the reaction process, fragments can be recognized by a minimum spanning tree (MST) algorithm, in which nucleons with relative distance of coordinate and momentum of $|r_i - r_j| \leqslant R_0$ and $|p_i - p_j| \leqslant P_0$ belong to a fragment [39]. R_0 and P_0 are phenomenological parameters with typical values $R_0 = 3.0$ fm and $P_0 = 250$ MeV/c being used in other quantum molecular dynamics (QMD) codes [39,48]. In this work, a slightly larger $R_0 = 3.5$ fm, together with $P_0 =$ 250 MeV/c, was found to best reproduce the experimental fragment multiplicities and production cross sections. The chosen values are in accordance with the potential range and large enough to permit recognizing the initial projectile and target at the beginning of the collision.

The excitation energy of the fragments can be calculated:

$$E^* = \frac{\sum_i U_i + \sum_i \frac{(\mathbf{p}_i - \mathbf{p}_f)^2}{2m} - B(Z_f, A_f)}{A_f}. \quad (8)$$

Here U_i and $\mathbf{p}_i$ are the single-particle potential and momentum of the ith nucleon; $\mathbf{p}_f$, Z_f, and A_f are the average momentum per nucleon, charge number, and mass number of the fragment; $B(Z_f, A_f)$ is the binding energy of a nucleus with charge number Z_f and mass number A_f. The summation is for the nucleons belonging to the same fragment.

The MST algorithm is performed during the collision. The outputted mass number and excitation energy of the heaviest fragment (or system) are shown in Fig. 1 as a function of time for collisions of ^{124}Sn + ^{120}Sn at 600 MeV/nucleon with the impact parameter of $b = 5$ fm. Note that we choose $t = 0$ fm/c to be the point of first contact between projectile and target, but the simulation of the reaction begins at -50 fm/c. At the beginning from -50 to 10 fm/c, the projectile is approaching the target. The heaviest fragment output by the MST algorithm is the projectile with mass number $A = 124$. The excitation energy rises very slowly due to collisions within the projectile but remains close to zero for $-50 \leqslant t < 10$ fm/c. During the dynamical and nonequilibrium stage from 10 to 40 fm/c, the projectile and target are no longer recognized as individual nuclei by the MST algorithm and the combined

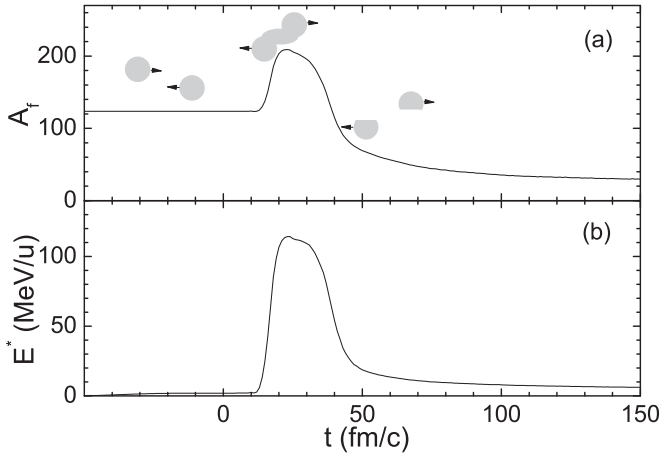

FIG. 1. Mass number and excitation energy of the heaviest fragment (or system) as a function of time in the collisions of ^{124}Sn + ^{120}Sn at 600 MeV/nucleon with the impact parameter of $b = 5$ fm. The evolution of the collision geometry is sketched in the top panel. The time $t = 0$ fm/c is chosen to be the point of first contact between projectile and target.

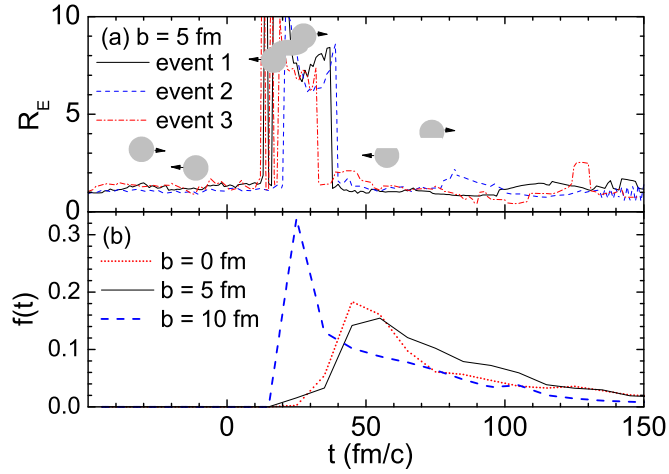

FIG. 2. (a) Time evolution of R_E of the heaviest fragment (or system) in three events of ^{124}Sn + ^{120}Sn collisions at 600 MeV/nucleon with the impact parameter of $b = 5$ fm. (b) Distribution of time when the projectile spectator achieves equilibrium in ^{124}Sn + ^{120}Sn collisions at 600 MeV/nucleon with impact parameters of $b = 0$, 5, and 10 fm.

system containing the full collision energy is obtained as the heaviest fragment. It is only after $t = 40$ fm/c that a projectile spectator and a target spectator can be distinguished. Because of the fragmentation of the excited spectators, the mass number and the excitation energy of the identified heaviest fragment decrease slowly. The MST method was also applied in QMD calculations to study the fragmentation of ^{197}Au projectiles after collisions with various targets at 600 MeV/nucleon [49] and in ^{197}Au + ^{197}Au collisions at incident energies of 400, 600, and 1000 MeV/nucleon [50] but the fragment production in collisions with medium and large impact parameters was underestimated in both studies. Those calculations also showed the separation of the projectile spectator and target spectator after the violent phase of the collisions. However, the transition between the nonequilibrium stage and fragmentation is continuous. The MST algorithm is unable to distinguish the onset of the equilibrated projectile spectator.

The ratio of parallel to transverse quantities is further used to distinguish the equilibrated projectile spectator:

$$R_E = \frac{2\sum_i (p_{zi} - p_{zf})^2}{\sum_i [(p_{xi} - p_{xf})^2 + (p_{yi} - p_{yf})^2]}, \quad (9)$$

where p_{xi}, p_{yi}, and p_{zi} are the momentum components of the ith nucleon along the x, y, and z axes; p_{xf}, p_{yf}, and p_{zf} are the average momentum per nucleon of the fragment along the x, y, and z axes. The summation is for the nucleons belonging to the same fragment. The z axis is the direction of incidence of the projectile. The value of R_E is 1 for an equilibrated system. The time evolution of R_E can be calculated for each event in the IQMD model. For example, in Fig. 2(a) the time evolution of R_E of the heaviest fragment is shown for three events of ^{124}Sn + ^{120}Sn collisions at 600 MeV/nucleon with the impact parameter of $b = 5$ fm. As mentioned above, the heaviest fragment at the beginning is the projectile. Thus the value of R_E is close to 1 at this stage. In the dynamical and nonequilibrium stage (from 10 to about 40 fm/c), the heaviest "fragment" is the colliding system, in which the parallel energy is close to the incident energy. We can see a very large value of R_E at this stage. After the projectile spectator is separated from the participant region, its value of R_E decreases and gets close to 1. Considering the observed fluctuation, the projectile spectator with a value of $0.9 < R_E < 1.2$ is regarded as equilibrated.

Figure 2(b) shows the distribution of time when the projectile spectator achieves equilibrium in ^{124}Sn + ^{120}Sn collisions at 600 MeV/nucleon with the impact parameters of $b = 0$, 5, and 10 fm. A total of 1×10^4 events are used to obtain this result. It can be seen that the time needed for equilibrium in the central ($b = 0$ fm), mid-peripheral ($b = 5$ fm), and peripheral ($b = 10$ fm) collisions is located in the interval $20 < t < 150$ fm/c. The most probable time needed for equilibrium for central and mid-peripheral collisions is about 50 fm/c. For peripheral collisions ($b = 10$ fm), inelastic reactions and the fragmentation occur simultaneously. The inelastic scattering results in a peak of the time distribution at $t = 25$ fm/c.

After the time for equilibration, the statistical description for the fragmentation is possible. However, the parameters, i.e., the excitation energies, mass numbers, and charges of the predicted equilibrated sources, are uncertain and model dependent. Figure 3 shows the mass of the equilibrated projectile spectator as a function of impact parameter in ^{124}Sn + ^{120}Sn collisions at 600 MeV/nucleon. For comparison, the mass of the projectile spectator is also calculated according to the participant-spectator geometry proposed by Gosset *et al.* [51]. The projectile and the target are assumed to be spherical with radii of 5.45 fm. Straight line trajectories for the projectile and target are applied. The participant-spectator geometry involves the calculation of the volume of intersection of a sphere and a cylinder. Within this approach, the mass of the equilibrated projectile spectator increases monotonously with increasing impact parameter. For the semi-central collision, the geometrical spectator appears in a crescent shape. Within the

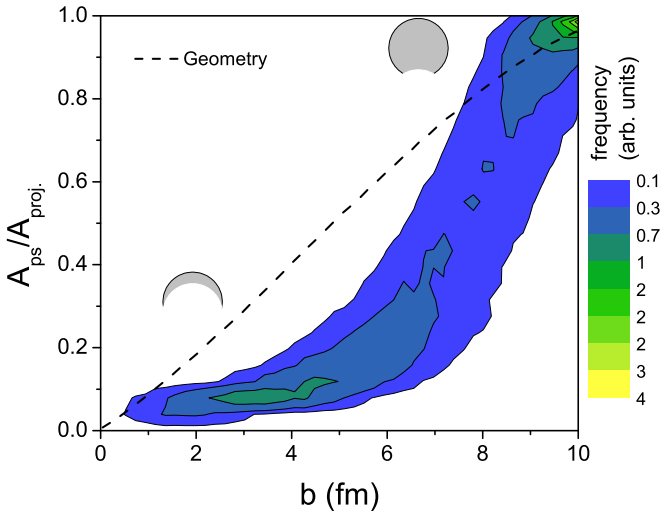

FIG. 3. Mass of the equilibrated projectile spectator as a function of impact parameter in ^{124}Sn + ^{120}Sn collisions at 600 MeV/nucleon. The mass is reduced to the mass of the projectile. The mass of the projectile spectator, calculated by geometrical analysis, is shown as a dashed curve.

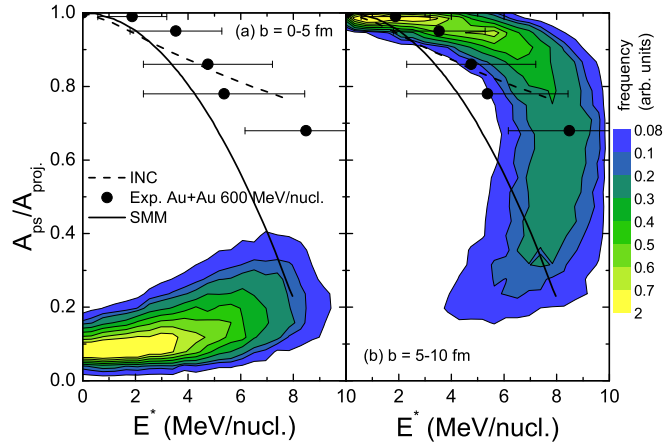

FIG. 5. Correlations between mass and excitation energy of the equilibrated projectile spectator from the simulation of ^{124}Sn + ^{120}Sn collisions at 600 MeV/nucleon with impact parameters ranging (a) from 0 to 5 fm and (b) from 5 to 10 fm. The mass is reduced to the mass of the projectile. The indicated INC prediction, SMM assumption, and experimental finding for Au/Au collisions [52] are taken from Ref. [53].

MST algorithm and Eq. (9), the dynamic spectator separated from the participant region can be distinguished. The spectator will emit nucleons before it is separated from the participant region. Thus we see in Fig. 3 that the dynamic mass is generally smaller than the mass according to the participant-spectator geometry except for small and very large impact parameters.

Figure 4 shows the excitation energy of the equilibrated projectile spectator as a function of impact parameter in ^{124}Sn + ^{120}Sn collisions at 600 MeV/nucleon. With increasing impact parameter, the excitation energy of the equilibrated projectile spectator rises and then falls. The excitation energy of the equilibrated projectile spectator reaches the largest value of 8 MeV/nucleon in collisions with impact parameter $b = 8$ fm. The fluctuation of the excitation energy is very large. For

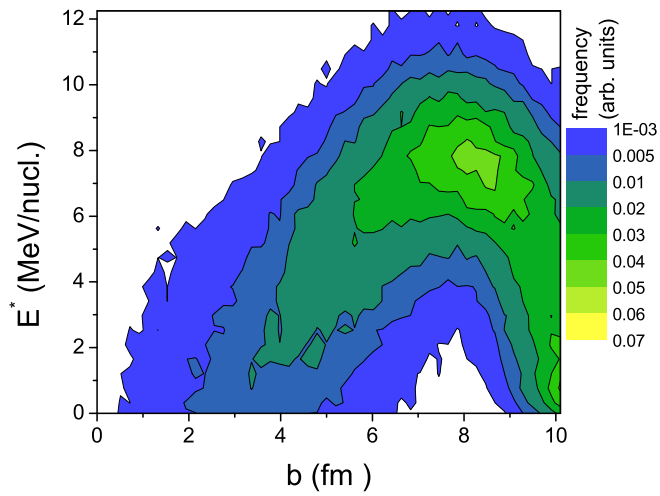

FIG. 4. Excitation energy of the equilibrated projectile spectator as a function of impact parameter in ^{124}Sn + ^{120}Sn collisions at 600 MeV/nucleon.

example, in collisions with $b = 8$ fm, the excitation energy is distributed over an interval from 2 to 12 MeV/nucleon. The center of the distribution is at 8 MeV/nucleon and coincides with the average binding energy of nuclei that has the same value. It means that the hot source is not bound. It will emit IMFs during its decay and reach the bound state.

The correlations between mass and excitation energy of the equilibrated projectile spectator are obtained from the simulation of ^{124}Sn + ^{120}Sn collisions at 600 MeV/nucleon with two impact parameter intervals, 0–5 and 5–10 fm (Fig. 5). In the figure, the indicated intranuclear cascade (INC) prediction, SMM assumption, and experimental finding for Au+Au collisions [52] are taken from Ref. [53]. The mass is reduced to the mass of the projectile. For $b = 0$–5 fm, the correlation of an increasing excitation energy with increasing mass is found. As mentioned above, the hot sources distinguished by the MST algorithm and Eq. (9) are the spectators after their separation from the participant region. During the separation process, the excitation energy of the spectator will decrease rapidly by nucleon emission or fragmentation. In other words, the hot sources for $b = 0$–5 fm are only recognized at a late time when kinematic equilibration is reached, possibly at a rather low level of excitation. It has the effect that the correlations between mass and excitation energy of the spectator for $b = 0$–5 fm are very different from what was found useful [53,54] or determined [55] in SMM analyses (solid curve in Fig. 5).

For $b = 5$–10 fm, the general correlation of an increasing excitation energy with a decreasing mass is observed for spectator masses for $A_{ps}/A_{\rm proj} > 0.7$. The hot sources with masses of $0.3 < A_{ps}/A_{\rm proj} < 0.7$ have excitation energies of about 8 MeV/nucleon. The error bars of the experimental distributions for Au+Au collisions at 600 MeV/nucleon reach the center of the distributions in this work. The results by the intranuclear cascade model are close to the lower bounds of the distributions in this work. Comparing the distributions in this work to that used in the SMM, we can find similarities only for

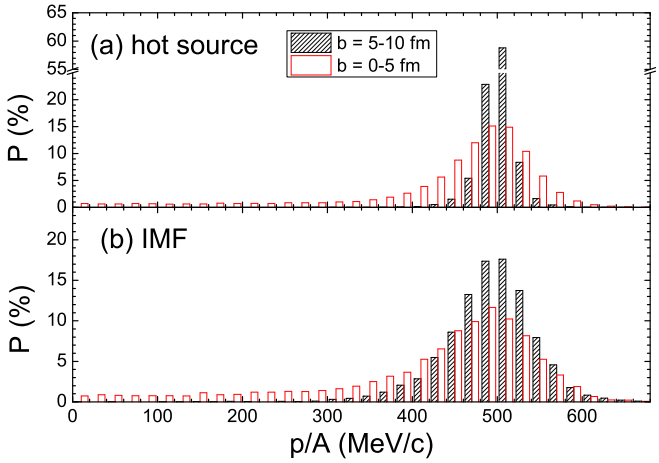

FIG. 6. Distributions of (a) the longitudinal momenta (c.m.) of the equilibrated projectile spectator in ^{124}Sn + ^{120}Sn collisions at 600 MeV/nucleon and (b) the asymptotic fragments for impact parameters b = 5–10 fm and 0–5 fm as indicated.

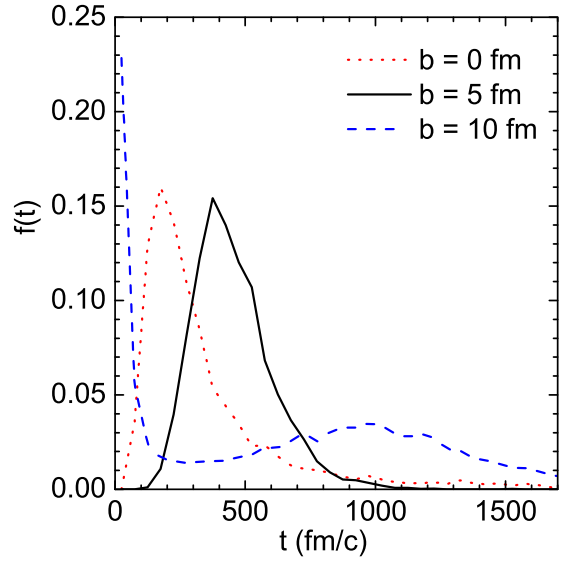

FIG. 7. Distribution of the switching time in ^{124}Sn + ^{120}Sn collisions at 600 MeV/nucleon for impact parameters of b = 0, 5, and 10 fm.

large and small masses. However, in the middle region, the hot sources predicted by the IQMD model have larger excitation energies than those applied in the SMM analyses.

To show whether the hot sources and IMFs come from the spectator region, we plot the distributions of longitudinal momenta of hot sources and IMFs for b=0–5 and 5–10 fm in Fig. 6. One can see that the hot sources extracted by the MST algorithm for b = 5–10 fm have momenta close to the projectile momentum (529 MeV/c). For b = 0–5 fm, some hot sources come from the participant region, since the distribution of momenta reaches down to zero. However, the percentage of the hot sources with momenta less than 300 MeV/c is smaller than 10%. That is to say, the MST algorithm works well when it distinguishes the spectator. The distributions of longitudinal momenta of IMFs are shown in Fig. 6(b). They are nearly Gaussian with a center near the projectile momentum for b = 5–10 fm, indicating that the IMFs mainly come from the spectator. For b = 0–5 fm, we see a similar Gaussian distribution, but with about 15% of the counts at p/A < 300 MeV/c. That is to say, about 15% of the IMFs come from the participant region for b = 0–5 fm.

B. Influence of secondary decay on fragmentation observables

In this section, the effects of sequential decay are studied by comparing calculations with and without the statistical code GEMINI. The crucial parameter to match the IQMD with GEMINI is the switching time, which represents the dynamical evolution time of the IQMD model before the GEMINI code is switched on. There are spurious emissions of nucleons in the IQMD model. It means that a few nucleons will be evaporated even if one simulates a single nucleus in its ground state. As the time proceeds and for lighter nuclei, this effect becomes stronger. In our previous work, the switching time was the same for central and peripheral collisions [56]. We chose the switching time so that the fragmentation in peripheral collisions has been completed. But for central collisions, the same switching time results in spurious nucleon emissions of prefragments. The IMFs produced in central collisions will falsely emit nucleons and possibly become free nucleons themselves if the evolution times are too long. In this work, to avoid the spurious emissions of nucleons and to preserve the number of prefragments, the evolution by IQMD will be stopped when the excitation energies of the two heaviest prefragments are less than a parameter $E_{\rm stop}$ that is determined from the onset of multifragmentation as observed in heavy-ion reactions. It has the consequence that the switching time, i.e., the dynamical evolution time until $E_{\rm stop}$ is reached, is different for each event. Figure 7 shows the distribution of the switching times in ^{124}Sn + ^{120}Sn collisions at 600 MeV/nucleon with the impact parameters of b = 0, 5, and 10 fm. A total of 1 × 10^4 events are used to obtain this result. It can be seen that the time distribution extends over a large region, from 50 to 1700 fm/c. Inelastic scattering and fragmentation result in two peaks for peripheral collisions (b = 10 fm). The peak at 50 fm/c refers to the inelastic scattering. The dynamical evolution is followed for times of the order of 1000 fm/c for peripheral collisions. Because the PSDC method is used, the inevitable spurious emissions are kept at a small level. Typically only about five nucleons are emitted spuriously from a cold ^{124}Sn nucleus during 2000 fm/c evolution time. Only about 200 fm/c dynamical evolution is simulated for central collisions. We preserve the number of prefragments for central collisions in contrast to our previous work [57].

To show the role of the GEMINI code, we compare the calculations in ^{124}Sn + ^{120}Sn collisions at 600 MeV/nucleon with the impact parameter of 5 fm performed with the IQMD alone and with the IQMD+GEMINI model in Fig. 8. Figures 8(a) and 8(b) show the excitation energy distribution and mass distribution of the largest fragment in an event. Figures 8(c) and 8(d) show distributions of the total bound charge in an event and the mean multiplicity as a function of the fragment charge Z. The outputs of the IQMD model without the GEMINI code represent the excited prefragments, while the outputs of

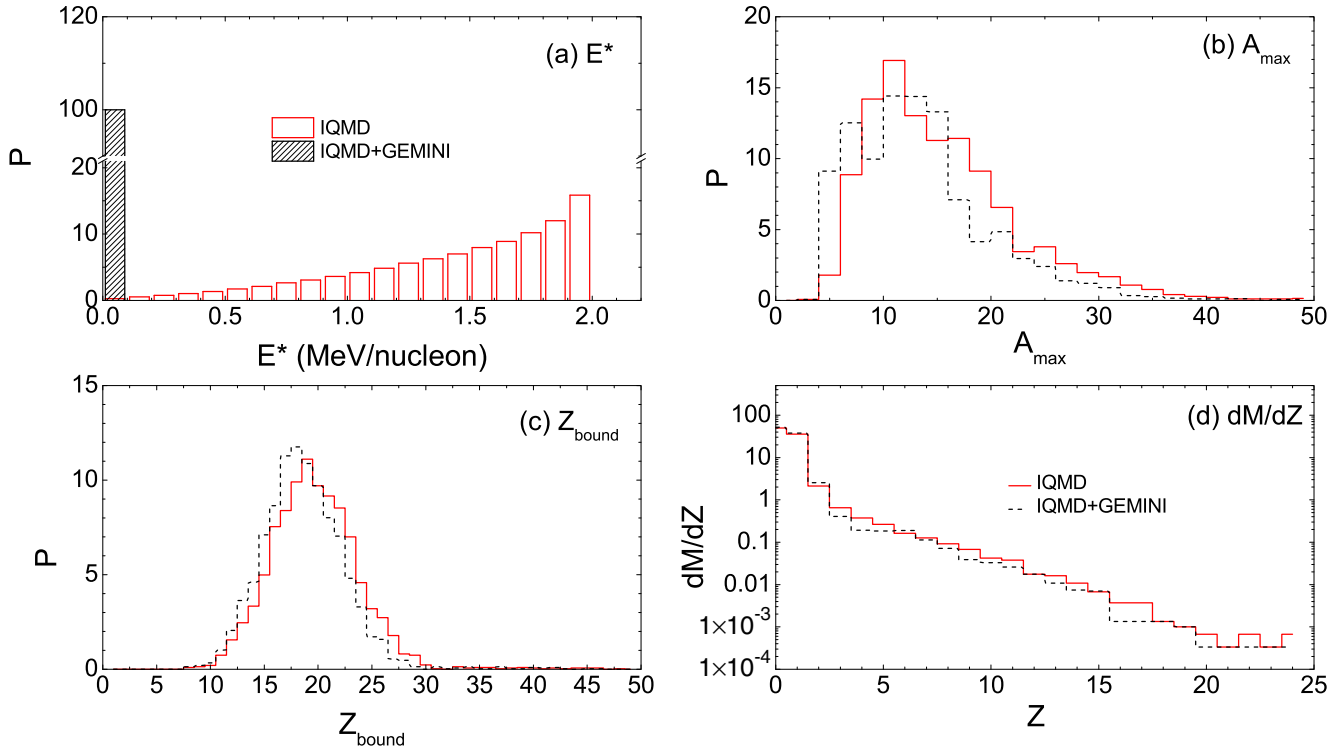

FIG. 8. Comparison between the calculations by IQMD and IQMD+GEMINI models in ^{124}Sn + ^{120}Sn collisions at 600 MeV/nucleon with the impact parameter of 5 fm for $E_{\rm stop}$ = 2 MeV. (a) Excitation energy distribution and (b) mass distribution of the largest fragment in an event. (c) Distribution of the total bound charge in an event and (d) distribution of the mean multiplicity as a function of the fragment charge Z.

the combined IQMD+GEMINI models are the final fragments. Because $E_{\rm stop}$ = 2 MeV/nucleon is used, the energies of the prefragments obtained with the IQMD are distributed across 0–2 MeV/nucleon. The excitation energies of all final fragments are zeero. Figures 8(b) and 8(c) show that the distributions of $A_{\rm max}$ and $Z_{\rm bound}$ by IQMD+GEMINI move slightly to the left compared with those from IQMD alone. There are fewer IMFs and more light particles ($Z < 3$) obtained with IQMD+GEMINI calculations than with the IQMD alone [Fig. 8(d)]. The nucleon evaporation of the prefragments is responsible for these results. In fact, by changing the symmetry of the fission mode, or by increasing the upper limit of the mass in the evaporation mode, the GEMINI code can also be used for studying the multifragmentation or spallation [58]. In this work, the multifragmentation mode in the GEMINI code is switched off, since we devote ourselves to studying the dynamic process of fragment production within the transport model. The GEMINI code is necessary, although it is not used to simulate the fragment production. We should compare the experimental data to the calculation of final fragments, but not the excited prefragments.

Figure 9 shows the mean multiplicity of IMFs ($3 \leqslant Z \leqslant 20$) as a function of $Z_{\rm bound}$ for the reaction of ^{124}Sn + ^{120}Sn at 600 MeV/nucleon by IQMD [Fig. 9(a)] and IQMD+GEMINI [Fig. 9(b)]. The experimental data for the same reaction, performed with a natural Sn target (atomic weight 118.7), are taken from Ref. [53]. The acceptance of the ALADIN forward spectrometer for projectile fragments is large. By studying angular distributions measured for the present reactions, it was found to increase with Z from about 90% for projectile fragments with $Z = 3$ to values exceeding 95% for $Z \geqslant 6$ [53]. In the calculations, fragments with $p_z > 0$ in the c.m. frame are retained, where p_z is the momentum in the incident direction. With this condition, all products forward of mid-rapidity are included into the projectile-spectator source. However, because most of the fragments are distributed around projectile rapidity (Fig. 6), we consider the minor effects caused by

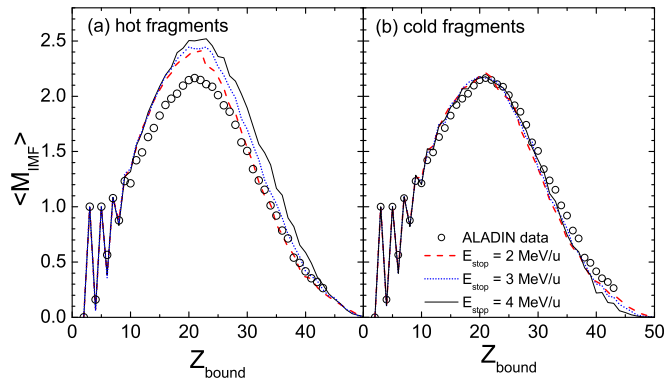

FIG. 9. Mean multiplicity of IMFs ($3 \leqslant Z \leqslant 20$) as a function of $Z_{\rm bound}$ for reactions of ^{124}Sn + ^{120}Sn at 600 MeV/nucleon by (a) IQMD and (b) IQMD+GEMINI. The calculations were performed for three values of $E_{\rm stop}$ as indicated. The experimental data (open circles) are taken from Ref. [53].

slower particles and by the spectrometer acceptance as not essential for the following comparison.

The multiplicities exhibit the rise and fall of the fragment production. The lower multiplicities for smaller values of $Z_{\rm bound}$ indicate the presence of vaporization events in central collisions, while those in the $Z_{\rm bound} = 50$ region indicate the inelastic events in peripheral collision. The data strongly stagger for $Z_{\rm bound} < 10$. This phenomenon is caused by the definition of $Z_{\rm bound}$ which includes the charge of observed α particles whose number is not included in $M_{\rm IMF}$. In particular, we observe that the MST method as applied in the present study is capable of reproducing the fragment production over the full range of $Z_{\rm bound}$, in contrast to Refs. [49,50]. The reason for the difference is not fully clear at present and will require further studies. Preliminary calculations indicate that it is related not to the MST parameters but possibly to the PSDC method chosen for modeling Pauli blocking.

Investigations of the average fragment multiplicity as a function of the excitation energy have shown that the onset of multifragmentation takes place for excitation energies around 3 MeV/nucleon [3]. We choose three values $E_{\rm stop} = 2$, 3, and 4 MeV/nucleon to match the IQMD with GEMINI. The calculations reproduce the rise and fall of the data. The IQMD model overestimates the multiplicity of IMFs, while the IQMD+GEMINI model reproduces it. Since the multifragmentation mode in the GEMINI code is switched off, the IMFs are not produced in the decay process of the prefragments. Moreover, some IMFs will decay to α particles. The IMF multiplicities delivered by IQMD+GEMINI are therefore slightly smaller than those by IQMD alone. We also see that the multiplicity of the final fragments does not visibly depend on the chosen $E_{\rm stop}$, except for very large $Z_{\rm bound}$. It indicates that the prefragments with excitation energies less than 4 MeV/nucleon decay predominantly by evaporation of nucleons in the IQMD model.

To study the isospin effect of the projectile fragmentation, we compare the mean multiplicity of IMFs as a function of $Z_{\rm bound}$ for reactions of ^{107}Sn + ^{120}Sn and ^{124}Sn + ^{120}Sn at 600 MeV/nucleon. The fragmentation of ^{107}Sn on natural Sn targets at this energy was studied by the ALADIN Collaboration with radioactive beams produced by the fragmentation of a primary ^{142}Nd beam [53]. The isotopic composition of the obtained secondary beams is presented and discussed in Ref. [59]. In Fig. 10, the mean multiplicity of IMFs is normalized with respect to the mass numbers of the projectiles. It is shown that the mean multiplicity of IMFs is very well reproduced by the IQMD+GEMINI model but $Z_{\rm bound}$ for the ^{107}Sn case is typically two units smaller than the experimental values. It corresponds to one α particle that, on average, seems to be missing in the calculated partitions relative to the experiment. The ALADIN data exhibit a small isospin effect. In the region $Z_{\rm bound} < 25$, the mean multiplicity of IMFs for ^{107}Sn fragmentation is slightly larger than that for ^{124}Sn fragmentation, while in the region $Z_{\rm bound} > 25$, the opposite phenomenon is observed. Both the calculations with and without GEMINI exhibit the same isospin effect with comparable magnitude. It seems that the sequential decay process does not strongly influence the isospin effect of projectile fragmentation.

Figure 11 shows the mean maximum charge normalized to the projectile charge Z_p as a function of the normalized

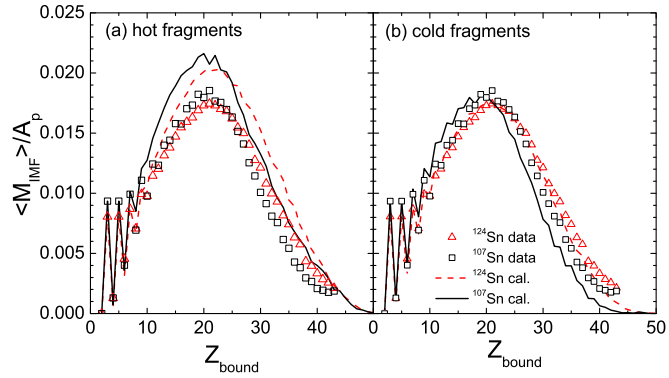

FIG. 10. Isospin effect of mean multiplicity of IMFs for reactions of ^{124}Sn, ^{107}Sn + ^{120}Sn at 600 MeV/nucleon by (a) IQMD and (b) IQMD+GEMINI. In the calculations, $E_{\rm stop} = 4$ MeV/nucleon is used. Experimental data are taken from Ref. [53].

bound charge $Z_{\rm bound}/Z_p$ for reactions of (a) ^{124}Sn + ^{120}Sn and (b) ^{107}Sn + ^{120}Sn at 600 MeV/nucleon. Experimental data [53] are shown as circles. With increasing $Z_{\rm bound}/Z_p$, the average charge of the heaviest fragment first slowly rises and then strongly increases, closing to the line of $Z_{\rm max}/Z_p = Z_{\rm bound}/Z_p$ at the end. The transition from predominantly residue production to multifragmentation appears as a reduction of $Z_{\rm max}/Z_p$ with respect to $Z_{\rm bound}/Z_p$, which occurs between $Z_{\rm bound}/Z_p = 0.6$ and 0.8. The agreement between calculations and data is very satisfactory overall and sufficient for performing the following analysis in individual intervals of $Z_{\rm bound}/Z_p$. The small discrepancy between calculations and data for ^{107}Sn is comparable to that observed for the correlation with the fragment multiplicity and corresponds to one missing α particle in the partition. Differences between the calculations with different $E_{\rm stop}$ are unapparent.

Figure 12 shows the cross sections $d\sigma/dZ$ for the fragments produced in the reaction of ^{124}Sn + ^{120}Sn at 600 MeV/nucleon. The data are shown as circles, while the calculations, performed with and without the use of GEMINI, are shown as lines. The bound charge $Z_{\rm bound}$ is known to

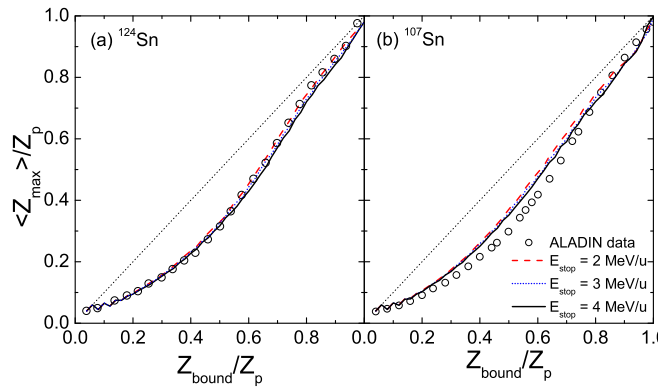

FIG. 11. Mean maximum charge normalized to the projectile charge Z_p as a function of $Z_{\rm bound}/Z_p$ for reactions of (a) ^{124}Sn + ^{120}Sn and (b) ^{107}Sn + ^{120}Sn at 600 MeV/nucleon. Experimental data are taken from Ref. [53].

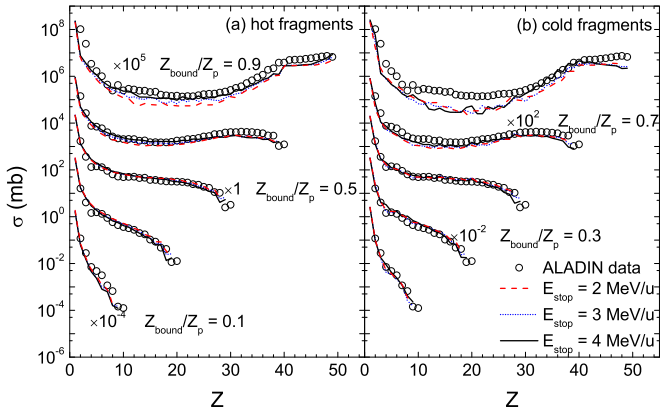

FIG. 12. Calculated cross sections $d\sigma/dZ$ for the fragments produced in the reaction of ^{124}Sn + ^{120}Sn at 600 MeV/nucleon, in comparison with the experimental data. The events are sorted into five intervals of $Z_{\rm bound}/Z_p$ with centers as indicated and width 0.2. The left panel shows the calculations with IQMD, and the right panel shows those with IQMD+GEMINI. Experimental data are taken from Ref. [53].

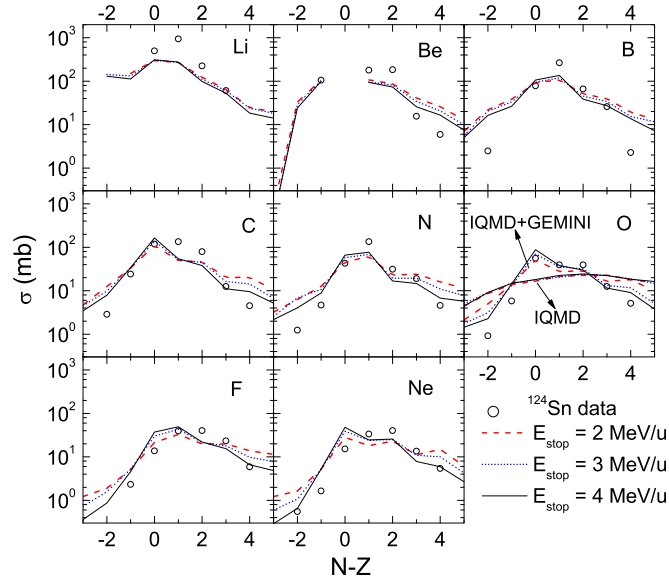

FIG. 13. Isotope distributions of fragments with $Z = 3$–10 for reactions of ^{124}Sn + ^{120}Sn at 600 MeV/nucleon. The calculations are obtained by the IQMD+GEMINI model. For comparison, the calculations of prefragments by IQMD are also shown for oxygen isotopes. The data are taken from Ref. [53].

monotonically correlate with the impact parameter of the reaction. A small $Z_{\rm bound}$ refers to more central collisions, while a large $Z_{\rm bound}$ indicates a more peripheral collision. The models can mainly reproduce the data, but underestimate the fragment cross section of the peripheral collisions. By studying the evolution of a single nucleus by the IQMD model, it was found that the nuclei are over-bounded by 1 MeV/nucleon [39]. The over-bound of the projectile in peripheral collisions is possibly responsible for the observed underestimation of the cross sections. The small dependence of the prefragment multiplicity on $E_{\rm stop}$ and its overestimation of the data, as exhibited in Fig. 9, is only partly recognized on the logarithmic scale of Fig. 12.

Figure 13 shows the isotope distributions of fragments with $Z = 3$–10 for reactions of ^{124}Sn + ^{120}Sn at 600 MeV/nucleon, again in comparison with the experimental data of Ref. [53]. We found that the effects of different $E_{\rm stop}$ are very small for the prefragments. The changes of the isotope distributions in the final evolution of the dynamic process, in which the excitation energies of the two heaviest prefragments decease from 4 to 2 MeV/nucleon, are apparently nearly negligible. As an example, we show the oxygen isotope distributions of prefragments by IQMD in the figure. They are practically independent of the chosen value of $E_{\rm stop}$. The sequential decay process leads to narrower isotope distributions, as can be seen by comparing the results with and without GEMINI. The excitation energy is a crucial parameter for GEMINI. Larger excitation energy ($E_{\rm stop} = 4$ MeV/nucleon) results in slightly narrower isotope distributions. The experimental values are better but still not well described when $E_{\rm stop} = 4$ MeV/nucleon is applied. Ricciardi *et al.* proposed that the nuclear structure can manifest itself in the decay stage of hot nuclei [60]. Here, the nuclear structure effects include the odd-even staggering and the dependence on asymmetry. The IQMD+GEMINI model produces a visible odd-even staggering and considerably narrower isotope distributions than IQMD alone (cf. the case of oxygen isotopes in Fig. 13). However, both effects are not as pronounced as observed in the experiment.

Figure 14 shows the isotope distributions of fragments with $Z = 3$–10 for reactions of ^{124}Sn, ^{107}Sn + ^{120}Sn at 600 MeV/nucleon. In the calculations, $E_{\rm stop} =$ 4 MeV/nucleon is used. The isospin dependence of the projectile fragmentation emerges in the isotope distributions. The

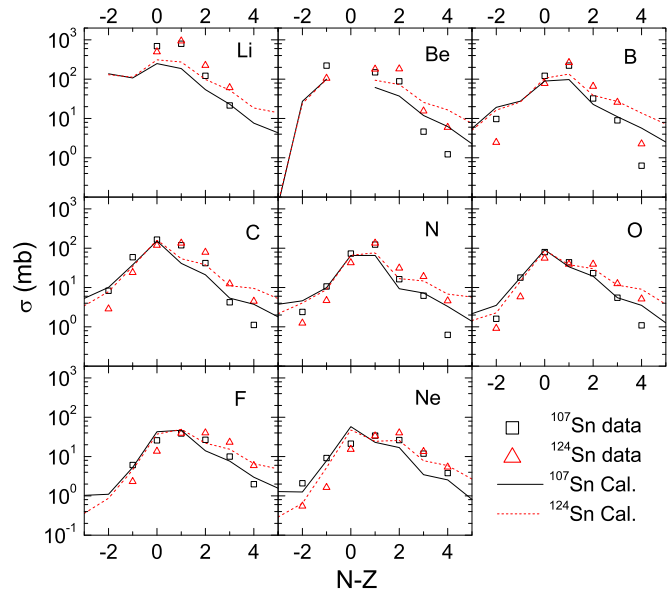

FIG. 14. Isospin effect of isotope distributions of fragments with $Z = 3$–10 for reactions of ^{124}Sn, ^{107}Sn + ^{120}Sn at 600 MeV/nucleon. In the calculations, $E_{\rm stop} = 4$ MeV/nucleon is used. The data are taken from Ref. [53].

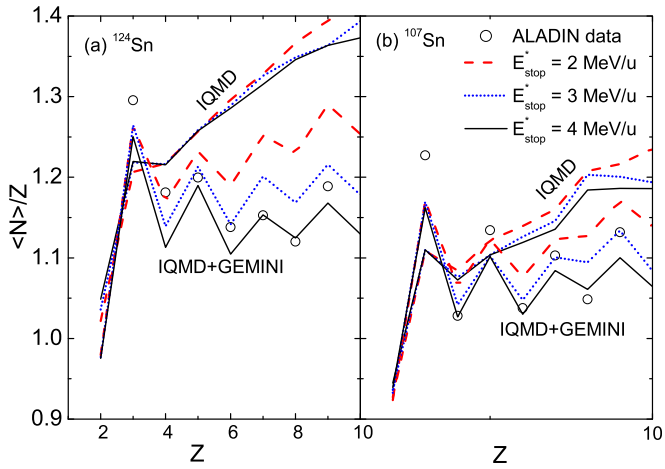

FIG. 15. Mean neutron-to-proton ratios $\langle N\rangle/Z$ of light fragments with $Z = 3$–9 for reactions of (a) ^{124}Sn + ^{120}Sn and (b) ^{107}Sn + ^{120}Sn at 600 MeV/nucleon. The data are taken from Ref. [2].

^{124}Sn fragmentation produces more neutron-rich fragments than ^{107}Sn fragmentation, while the opposite is the case for the production of neutron-poor fragments. These features are qualitatively reproduced.

The secondary decay effects can also be investigated on the basis of the neutron-to-proton ratios of the fragments. Figure 15 shows the mean neutron-to-proton ratios $\langle N\rangle/Z$ of light fragments with $Z = 3$–9 for reactions of (a) ^{124}Sn + ^{120}Sn and (b) ^{107}Sn + ^{120}Sn at 600 MeV/nucleon. The data, taken from Ref. [2], show obvious odd-even staggering. Both the values and the odd-even staggerings of the mean neutron-to-proton ratios are isospin dependent. The larger values of $\langle N\rangle/Z$ indicate that more neutron-rich nuclei are produced in projectile fragmentation of ^{124}Sn than of ^{107}Sn. The odd-even staggering is much more pronounced in the case of the ^{107}Sn fragmentation. Comparing the calculations with and without GEMINI, it is found that the secondary decay has a strong effect on $\langle N\rangle/Z$ in the case of the neutron-rich projectile. The mean neutron-to-proton ratio of the prefragments increases with Z. It probably reaches the value of 1.48 for the ^{124}Sn projectile asymptotically but exceeds the value of 1.14 of the projectile for ^{107}Sn. The neutron-deficient ^{107}Sn, possibly attracted by the valley of stability with $\langle N\rangle/Z = 1.37$ in the Sn region, may lose a few protons at the early stage of the collision.

The strongly bound nuclei (β-stable or even nuclei) attract a large fraction of the product yields during the secondary evaporation stage, resulting in smaller $\langle N\rangle/Z$ and the significant odd-even staggering of the calculations with GEMINI included. With the higher value, $E_{\rm stop} = 3$ or 4 MeV, the experimental result is remarkably well reproduced. The large shift in $\langle N\rangle/Z$ is already apparent in the case of oxygen shown in Fig. 13.

In Ref. [3], it is proposed that the threshold energy of the multifragmentation is close to 3 MeV/nucleon. The investigation of secondary decay effects of light fragments supports a similar value, $E_{\rm stop} = 4$ MeV/nucleon (Figs. 14 and 15). It is, therefore, not obvious why the odd-even staggering and the narrowing of the isotope distributions are underestimated by the calculations. Decays of hot fragments with excitation energies larger than 1 MeV/nucleon are expected to exhibit these structure effects [56]. The reason may be related to the fact that a fraction of prefragments may have reached excitation energies much smaller than $E_{\rm stop}$ before they were sent to GEMINI for the treatment of the final decays. That is to say, the secondary evaporation of a fraction of prefragments is simulated with the IQMD model, in which mean field without pairing energy is applied. Thus, the odd-even staggering of the light fragments is underestimated by the IQMD and GEMINI models when coupled in the present form.

IV. CONCLUSION

The projectile fragmentations of ^{107,124}Sn on ^{120}Sn at 600 MeV/nucleon was investigated within the framework of the IQMD model. The MST algorithm and the ratio of parallel to transverse quantities are applied to distinguish the equilibrated projectile spectator. It is found that the time needed for equilibrium being reached by the projectile spectator is located in the interval from 20 to 150 fm/c. The mass and excitation energy of the equilibrated projectile spectator are extracted. For impact parameters $b = 0$–5 fm, the MST algorithm and the ratio of parallel to transverse quantities distinguish the spectators at a late time when kinematic equilibration is reached. It is the reason why the obtained correlation of the spectator mass and excitation energy are so different from what was successfully used in statistical descriptions. For impact parameters $b = 5$–10 fm, the observed general correlation of an increasing excitation energy with a decreasing spectator mass is similar to those used in SMM analyses.

The influence of secondary decay on fragmentation observables was investigated by comparing the calculations with and without the statistical code GEMINI. The evolution by the IQMD model is stopped when the excitation energies of the two heaviest prefragments are less than $E_{\rm stop}$, which corresponds to the threshold energy of the multifragmentation. Then the GEMINI code is applied to study the secondary decay of the prefragments. It is found that the nucleon evaporations of the prefragments reduce the multiplicity of intermediate-mass fragments slightly, but do not change its dependence on the isospin of the projectile. The sequential decay also leads to narrower isotope distributions but, generally, not as narrow as observed experimentally. Larger $E_{\rm stop}$ results in slightly narrower isotope distributions.

It is demonstrated that by permitting only evaporation in GEMINI, the IQMD+GEMINI model is able to reproduce the main features of projectile fragmentation. In particular, it is observed that the MST method as applied in the present study is capable of reproducing the fragment production over the full range of $Z_{\rm bound}$. The reason for the difference from previous work is not fully clear at present and will require further studies. Regarding the isotopic effects, the evaporation is sufficient to restore the mean neutron-to-proton ratios and odd-even staggering of the light fragments, but not the widths of the mass distributions.

ACKNOWLEDGMENTS

This work was supported by the National Natural Science Foundation of China under Grants No. 11405278, No.

11605296, No. 11505150, and No. 11635003, the Natural Science Foundation of Guangdong Province China under Grant No. 2016A030310208, and the China Postdoctoral Science Foundation under Grant No. 2015M582730. The authors are grateful to the ALADIN Collaboration for providing the numerical values of experimental results reported in Ref. [53].

[1] C. Y. Wong and K. Van Bibber, Phys. Rev. C **25**, 2990 (1982).
[2] W. Trautmann, P. Adrich, T. Aumann, C. O. Bacri, T. Barczyk, R. Bassini, S. Bianchin, C. Boiano, A. S. Botvina, A. Boudard, J. Brzychczyk, A. Chbihi, J. Cibor, B. Czech, M. De Napoli, J.-É. Ducret, H. Emling, J. D. Frankland, M. Hellström, D. Henzlova, G. Immè, I. Iori, H. Johansson, K. Kezzar, A. Lafriakh, A. Le Fèvre, E. Le Gentil, Y. Leifels, J. Lühning, J. Łukasik, W. G. Lynch, U. Lynen, Z. Majka, M. Mocko, W. F. J. Müller, A. Mykulyak, H. Orth, A. N. Otte, R. Palit, P. Pawłowski, A. Pullia, G. Raciti, E. Rapisarda, H. Sann, C. Schwarz, C. Sfienti, H. Simon, K. Sümmerer, M. B. Tsang, G. Verde, C. Volant, M. Wallace, H. Weick, J. Wiechula, A. Wieloch, and B. Zwiegliński, Int. J. Mod. Phys. E **17**, 1838 (2008).
[3] B. Borderie and M. F. Rivet, Prog. Part. Nucl. Phys. **61**, 551 (2008).
[4] M. A. Jilany, Phys. Rev. C **70**, 014901 (2004).
[5] P. Napolitani, K.-H. Schmidt, A. S. Botvina, F. Rejmund, L. Tassan-Got, and C. Villagrasa, Phys. Rev. C **70**, 054607 (2004).
[6] B. K. Singh and S. K. Tuli, Nuovo Cimento A **112**, 1093 (1999).
[7] D. Pérez-Loureiro, J. Benlliure, H. Álvarez-Pol, B. Blank, E. Casarejos, D. Dragosavac, V. Föhr, M. Gascón, W. Gawlikowicz, A. Heinzf, K. Helariutta, A. Kelić-Heil, S. Lukić, F. Montes, L. Pieńkowski, K.-H. Schmidt, M. Staniou, K. Subotić, K. Sümmerer, J. Taieb, and A. Trzcińska, Phys. Lett. B **703**, 552 (2011).
[8] K. Minamisono, D. M. Rossi, R. Beerwerth, S. Fritzsche, D. Garand, A. Klose, Y. Liu, B. Maaß, P. F. Mantica, A. J. Miller, P. Müller, W. Nazarewicz, W. Nörtershäuser, E. Olsen, M. R. Pearson, P.-G. Reinhard, E. E. Saperstein, C. Sumithrarachchi, and S. V. Tolokonnikov, Phys. Rev. Lett. **117**, 252501 (2016).
[9] M. Belleguic, M. J. Lopez-Jimenez, M. Stanoiu, F. Azaiez, M. G. Saint-Laurent, O. Sorlin, N. L. Achouri, J. C. Angélique, C. Borcea, C. Bourgeois, J. M. Daugas, C. Donzaud, F. De Oliveira-Santos, Z. Dlouhy, J. Duprat, S. Grevy, D. Guillemaud-Mueller, S. Leenhardt, M. Lewitowicz, W. Mittig, A. C. Mueller, N. Orr, Yu.-E. Penionzhkevich, M. G. Porquet, F. Pougheon, P. Roussel-Chomaz, J. E. Sauvestre, H. Savajols, and Yu. Sobolev, Phys. Scr. T **88**, 122 (2000).
[10] K. Yoneda, H. Sakurai, T. Gomi, T. Motobayashi, N. Aoi, N. Fukuda, U. Futakami, Z. Gacsi, Y. Higurashi, N. Imai, N. Iwasa, H. Iwasaki, T. Kubo, M. Kunibu, M. Kurokawa, Z. Liu, T. Minemura, A. Saito, M. Serata, S. Shimoura, S. Takeuchi, Y. X. Watanabe, K. Yamada, Y. Yanagisawa, K. Yogo, A. Yoshida, and M. Ishihara, Phys. Lett. B **499**, 233 (2001).
[11] E. Bonnet, D. Mercier, B. Borderie, F. Gulminelli, M. F. Rivet, B. Tamain, R. Bougault, A. Chbihi, R. Dayras, J. D. Frankland, E. Galichet, F. Gagnon-Moisan, D. Guinet, P. Lautesse, J. Łukasik, N. Le Neindre, M. Pârlog, E. Rosato, R. Roy, M. Vigilante, J. P. Wieleczko, and B. Zwieglinski, Phys. Rev. Lett. **103**, 072701 (2009).
[12] C. W. Ma, L. Huang, and Y. D. Song, Phys. Rev. C **95**, 024612 (2017).
[13] M. V. Ricciardi, T. Enqvist, J. Pereira, J. Benlliure, M. Bernas, E. Casarejos, V. Henzl, A. Kelić, J. Taïeb, and K.-H. Schmidt, Phys. Rev. Lett. **90**, 212302 (2003).
[14] H. H. Heckman, D. E. Greiner, P. J. Lindstrom, and F. S. Bieser, Science **174**, 1130 (1971).
[15] H. A. Grunder, W. D. Hartsough, and E. J. Lofgren, Science **174**, 1128 (1971).
[16] K. Sümmerer and B. Blank, Phys. Rev. C **61**, 034607 (2000).
[17] O. Tarasov, Nucl. Phys. A **734**, 536 (2004).
[18] K. Meierbachtol, D. J. Morrissey, M. Mosby, and D. Bazin, Phys. Rev. C **85**, 034608 (2012).
[19] Zs. Podolyák, J. Gerl, M. Hellström, F. Becker, K. A. Gladnishki, M. Górska, A. Kelić, Y. Kopatch, S. Mandal, P. H. Regan, K.-H. Schmidt, P. M. Walker, H. J. Wollersheim, A. Banu, G. Benzoni, H. Boardman, E. Casarejos, J. Ekman, H. Geissel, H. Grawe, D. Hohn, I. Kojouharov, J. Leske, R. Lozeva, M. N. Mineva, G. Neyens, R. D. Page, C. J. Pearson, M. Portillo, D. Rudolph, N. Saito, H. Schaffner, D. Sohler, K. Sümmerer, J. J. Valiente-Dobón, C. Wheldon, H. Weick, and M. Winkler, Phys. Lett. B **632**, 203 (2006).
[20] S. Pal and R. Palit, Phys. Lett. B **665**, 164 (2008).
[21] S. Das Gupta, S. Mallik, and G. Chaudhuri, Phys. Lett. B **726**, 427 (2013).
[22] M. Mocko, M. B. Tsang, Z. Y. Sun, N. Aoi, J. M. Cook, F. Delaunay, M. A. Famiano, H. Hui, N. Imai, H. Iwasaki, W. G. Lynch, T. Motobayashi, M. Niikura, T. Onishi, A. M. Rogers, H. Sakurai, A. Stolz, H. Suzuki, E. Takeshita, S. Takeuchi, and M. S. Wallace, Phys. Rev. C **76**, 014609 (2007).
[23] J. Benlliure, K.-H. Schmidt, D. Cortina-Gil, T. Enqvist, F. Farget, A. Heinz, A. R. Junghans, J. Pereira, and J. Taieb, Nucl. Phys. A **660**, 87 (1999).
[24] COFRA, http://www.usc.es/genp/cofra.
[25] B. Mei, Phys. Rev. C **95**, 034608 (2017).
[26] C. W. Ma, H. L. Wei, J. Y. Wang, G. J. Liu, Y. Fu, D. Q. Fang, W. D. Tian, X. Z. Cai, H. W. Wang, and Y. G. Ma, Phys. Rev. C **79**, 034606 (2009).
[27] J. P. Bondorf, A. S. Botvina, A. S. Iljinov, I. N. Mishustin, and K. Sneppen, Phys. Rep. **257**, 133 (1995).
[28] C. B. Das, S. Das Gupta, W. G. Lynch, A. Z. Mekjian, and M. B. Tsang, Phys. Rep. **406**, 1 (2005).
[29] S. Mallik, G. Chaudhuri, and S. Das Gupta, Phys. Rev. C **84**, 054612 (2011).
[30] R. J. Charity, M. A. McMahan, G. J. Wozniak, R. J. McDonald, L. G. Moretto, D. G. Sarantites, L. G. Sobotka, G. Guarino, A. Pantaleo, L. Fiore, A. Gobbi, and K. D. Hildenbrand, Nucl. Phys. A **483**, 371 (1988).
[31] G. F. Bertsch and S. Das Gupta, Phys. Rep. **160**, 189 (1988).
[32] Ch. Hartnack, Rajeev K. Puri, J. Aichelin, J. Konopka, S. A. Bass, H. Stöcker, and W. Greiner, Eur. Phys. J. A **1**, 151 (1998).
[33] T. Gaitanos, H. Lenske, and U. Mosel, Phys. Lett. B **675**, 297 (2009).
[34] J. Pu, J. H. Chen, S. Kumar, Y. G. Ma, C. W. Ma, and G. Q. Zhang, Phys. Rev. C **87**, 047603 (2013).

[35] Z. T. Dai, D. Q. Fang, Y. G. Ma, X. G. Cao, G. Q. Zhang, and W. Q. Shen, Phys. Rev. C **91**, 034618 (2015).
[36] D. Lacroix, A. Van Lauwe, and D. Durand, Phys. Rev. C **69**, 054604 (2004).
[37] A. Ono and H. Horiuchi, Prog. Part. Nucl. Phys. **53**, 501 (2004).
[38] M. Mocko, M. B. Tsang, D. Lacroix, A. Ono, P. Danielewicz, W. G. Lynch, and R. J. Charity, Phys. Rev. C **78**, 024612 (2008).
[39] J. Aichelin, Phys. Rep. **202**, 233 (1991).
[40] J. Su, K. Cherevko, W.-J. Xie, and F.-S. Zhang, Phys. Rev. C **89**, 014619 (2014).
[41] J. Xu, L. W. Chen, M. Y. B. Tsang, H. Wolter, Y. X. Zhang, J. Aichelin, M. Colonna, D. Cozma, P. Danielewicz, Z. Q. Feng, A. Le Fèvre, T. Gaitanos, C. Hartnack, K. Kim, Y. Kim, C. M. Ko, B. A. Li, Q. F. Li, Z. X. Li, P. Napolitani, A. Ono, M. Papa, T. Song, J. Su, J. L. Tian, N. Wang, Y. J. Wang, J. Weil, W. J. Xie, F. S. Zhang, and G. Q. Zhang, Phys. Rev. C **93**, 044609 (2016).
[42] M. B. Tsang, Y. X. Zhang, P. Danielewicz, M. Famiano, Zhuxia Li, W. G. Lynch, and A. W. Steiner, Phys. Rev. Lett. **102**, 122701 (2009).
[43] J. Cugnon, D. L'Hôte, and J. Vandermeulen, Nucl. Instrum. Methods Phys. Res. B **111**, 215 (1996).
[44] D. D. S. Coupland, W. G. Lynch, M. B. Tsang, P. Danielewicz, and Y. X. Zhang, Phys. Rev. C **84**, 054603 (2011).
[45] P. Danielewicz, Acta. Phys. Pol. B **33**, 45 (2002).
[46] M. Papa, T. Maruyama, and A. Bonasera, Phys. Rev. C **64**, 024612 (2001).
[47] J. Su and F. S. Zhang, Phys. Rev. C **87**, 017602 (2013).
[48] Y. Zhang and Z. Li, Phys. Rev. C **71**, 024604 (2005).
[49] M. Begemann-Blaich, W. F. J. Müller, J. Aichelin, J. C. Adloff, P. Bouissou, J. Hubele, G. Imme, I. Iori, P. Kreutz, G. J. Kunde, S. Leray, V. Lindenstruth, Z. Liu, U. Lynen, R. J. Meijer, U. Milkau, A. Moroni, C. Ngô, C. A. Ogilvie, J. Pochodzalla, G. Raciti, G. Rudolf, H. Sann, A. Schüttauf, W. Seidel, L. Stuttge, W. Trautmann, and A. Tucholski, Phys. Rev. C **48**, 610 (1993).
[50] Y. K. Vermani and Rajeev K. Puri, Europhys. Lett. **85**, 62001 (2009).
[51] J. Gosset, H. H. Gutbrod, W. G. Meyer, A. M. Poskanzer, A. Sandoval, R. Stock, and G. D. Westfall, Phys. Rev. C **16**, 629 (1977).
[52] J. Pochodzalla, T. Möhlenkamp, T. Rubehn, A. Schüttauf, A. Wörner, E. Zude, M. Begemann-Blaich, Th. Blaich, H. Emling, A. Ferrero, C. Gross, G. Immé, I. Iori, G. J. Kunde, W. D. Kunze, V. Lindenstruth, U. Lynen, A. Moroni, W. F. J. Müller, B. Ocker, G. Raciti, H. Sann, C. Schwarz, W. Seidel, V. Serfling, J. Stroth, W. Trautmann, A. Trzcinski, A. Tucholski, G. Verde, and B. Zwieglinski, Phys. Rev. Lett. **75**, 1040 (1995).
[53] R. Ogul, A. S. Botvina, U. Atav, N. Buyukcizmeci, I. N. Mishustin, P. Adrich, T. Aumann, C. O. Bacri, T. Barczyk, R. Bassini, S. Bianchin, C. Boiano, A. Boudard, J. Brzychczyk, A. Chbihi, J. Cibor, B. Czech, M. De Napoli, J.-É. Ducret, H. Emling, J. D. Frankland, M. Hellström, D. Henzlova, G. Immè, I. Iori, H. Johansson, K. Kezzar, A. Lafriakh, A. Le Fèvre, E. Le Gentil, Y. Leifels, J. Lühning, J. Łukasik, W. G. Lynch, U. Lynen, Z. Majka, M. Mocko, W. F. J. Müller, A. Mykulyak, H. Orth, A. N. Otte, R. Palit, P. Pawłowski, A. Pullia, G. Raciti, E. Rapisarda, H. Sann, C. Schwarz, C. Sfienti, H. Simon, K. Sümmerer, W. Trautmann, M. B. Tsang, G. Verde, C. Volant, M. Wallace, H. Weick, J. Wiechula, A. Wieloch, and B. Zwiegliński, Phys. Rev. C **83**, 024608 (2011); **85**, 019903(E) (2012).
[54] A. S. Botvina, I. N. Mishustin, M. Begemann-Blaich, J. Hubele, G. Imme, I. Iori, P. Kreutz, G. J. Kunde, W. D. Kunze, V. Lindenstruth, U. Lynen, A. Moroni, W. F. J. Müller, C. A. Ogilvie, J. Pochodzalla, G. Raciti, Th. Rubehn, H. Sann, A. Schüttauf, W. Seidel, W. Trautmann, and A. Wörner, Nucl. Phys. A **584**, 737 (1995).
[55] P. Désesquelles, J. P. Bondorf, I. N. Mishustin, and A. S. Botvina, Nucl. Phys. A **604**, 183 (1996).
[56] J. Su, F. S. Zhang, and B. A. Bian, Phys. Rev. C **83**, 014608 (2011).
[57] J. Su and F. S. Zhang, Phys. Rev. C **84**, 037601 (2011).
[58] E. Le Gentil, T. Aumann, C. O. Bacri, J. Benlliure, S. Bianchin, M. Böhmer, A. Boudard, J. Brzychczyk, E. Casarejos, M. Combet, L. Donadille, J. E. Ducret, M. Fernandez-Ordoñez, R. Gernhäuser, H. Johansson, K. Kezzar, T. Kurtukian-Nieto, A. Lafriakh, F. Lavaud, A. Le Fèvre, S. Leray, J. Lühning, J. Lukasik, U. Lynen, W. F. J. Müller, P. Pawlowski, S. Pietri, F. Rejmund, C. Schwarz, C. Sfienti, H. Simon, W. Trautmann, C. Volant, and O. Yordanov, Phys. Rev. Lett. **100**, 022701 (2008).
[59] J. Łukasik, P. Adrich, T. Aumann, C. O. Bacri, T. Barczyk, R. Bassini, S. Bianchin, C. Boiano, A. S. Botvina, A. Boudard, J. Brzychczyk, A. Chbihi, J. Cibor, B. Czech, J.-É. Ducret, H. Emling, J. Frankland, M. Hellström, D. Henzlova, G. Immè, I. Iori, H. Johansson, K. Kezzar, A. Lafriakh, A. Le Fèvrea, E. Le Gentil, Y. Leifels, J. Lühning, W. G. Lynch, U. Lynen, Z. Majka, M. Mocko, W. F. J. Müller, A. Mykulyak, M. De Napoli, H. Orth, A. N. Otte, R. Palit, P. Pawłowski, A. Pullia, G. Raciti, E. Rapisarda, H. Sann, C. Schwarz, C. Sfienti, H. Simon, K. Sümmerer, W. Trautmann, M. B. Tsang, G. Verde, C. Volant, M. Wallace, H. Weick, J. Wiechula, A. Wieloch, and B. Zwiegliński, Nucl. Instrum. Methods A **587**, 413 (2008).
[60] M. V. Ricciardi, A. V. Ignatyuk, A. Kelić, P. Napolitani, F. Rejmund, K.-H. Schmidt, and O. Yordanov, Nucl. Phys. A **733**, 299 (2004).